Simulations of rare-isotope beams for the HISPEC/DESPEC experiments at the Super-FRS

J. Vesić [a,b,*], S. Saha [b,d], M. Górska [b], P. Boutachkov [b], G. Benzoni [c], J. Gerl [b], H. Weick [b], J. Winfield [b,1], S. Pietri [b], C. Nociforo [b], N. Pietralla [d], G. Guastalla [b,d], M. Winkler [b], H. Geissel [b]

[a] *Jožef Stefan Institute, Ljubljana, Slovenia*
[b] *GSI Helmholtzzentrum für Schwerionenforschung, Darmstadt, Germany*
[c] *INFN sezione di Milano, Milano, Italy*
[d] *Technische Universität Darmstadt, Darmstadt, Germany*

ABSTRACT

The HISPEC/DESPEC collaboration envisages long experimental campaigns exploiting the expected beam performances of Super-FRS. The experiments will be performed at the Low-Energy Branch of the upcoming FAIR and will focus on the physics of exotic isotopes, primarily in the heavy neutron-rich region. The goal of the HISPEC/DESPEC experimental campaigns is to explore the excitation and decay properties of rare isotopes produced via fragmentation and fission. First rare-isotope beam simulations of representative future HISPEC/DESPEC experimental cases are presented. The simulations provide an insight into the forthcoming state-of-art experiments in the future FAIR facility.

1. Introduction

The High-resolution In-flight SPECtroscopy/DEcay SPECtroscopy (HISPEC/DESPEC, H/D) experiments [1,2] will be carried out at the Low-Energy Branch (LEB) of the Superconducting Fragment Separator (Super-FRS) [3,4] of the upcoming Facility for Antiproton and Ion Research (FAIR) [5]. FAIR is currently being built at the site of the present GSI Helmholtzzentrum für Schwerionenforschung (GSI) in Darmstadt (Germany). The physics cases for the H/D experiments are part of the overall NUclear STructure, Astrophysics and Reactions program (NUSTAR), one of the four scientific pillars of FAIR.

H/D is built around a large suite of detectors to study several properties of rare isotopes produced via fragmentation and fission reactions at relativistic energies up to 1.5 GeV/u. High energies help to obtain these nuclei in the fully stripped state, thus avoiding any charge state ambiguity in the selection process with magnetic spectrometers [6].

HISPEC experiments aim at performing detailed spectroscopic studies by measuring outgoing γ radiation via various reactions induced by the Coulomb force and strong interaction. The core of the HISPEC setup is the Advanced GAmma Tracking Array (AGATA) [7], the latest generation array of segmented High-purity Germanium (HPGe) detectors, able to reconstruct the initial energy of the emitted γ radiation also in case of large Doppler displacement caused by the relativistic energies at play. AGATA is coupled to ancillary detectors for specific measurements (e.g. plunger devices for lifetimes determination, neutron

detectors etc.). The outgoing radioactive fragments will be identified event-by-event by time-of-flight (TOF). Energy loss and total energy will be measured in LYCCA (Lund-York-Cologne CAlorimeter) [8] in the final stage of the HISPEC set-up in conjunction with a magnetic spectrometer.

DESPEC experiments aim at a detailed study of the decay mechanism in the most exotic nuclear species at reach at FAIR, with the measurements of decay half-lives, competing decay modes and isomeric states identification. For the DESPEC experimental program, ions will be stopped in an Advanced Implantation Detector Array (AIDA) [9] and their subsequent decays measured. AIDA will be surrounded by a modular and compact high-resolution γ-ray array DEGAS [10] (DEspec Germanium Array Spectrometer) as well as the neutron array MONSTER (MOdular Neutron time of flight SpectromeTER) [11] and Beta-dELayEd Neutron detector (BELEN) [12]. In addition, the Decay Total Absorption Spectrometer (DTAS) [13] and the FAst TIMing Array (FATIMA) [14] will be employed.

The aforementioned set-ups will address key open questions in nuclear structure, reactions and nuclear astrophysics, when employed with the unique rare isotope beams delivered by the Super-FRS facility of FAIR.

The FAIR facility will produce intense, high energy beams of all stable elements up to uranium, using the existing linear accelerator (UNILAC) and synchrotron (SIS18) at GSI as injector, together with the
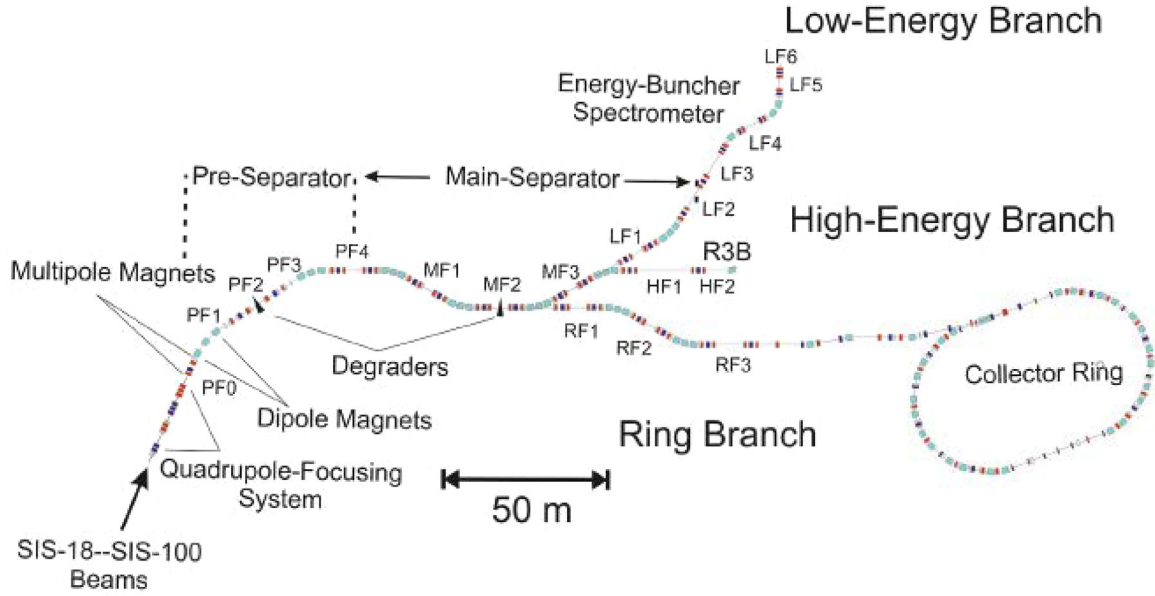
Fig. 1. Layout of the magnetic system of the Super-FRS with the principal ion-optical elements labeled. Dipoles are depicted in light blue color, quadrupoles focusing in vertical direction in dark blue color, quadrupoles focusing in horizontal direction are depicted in red color. Degraders are depicted in black color. The relevant parts of Super-FRS for H/D experiments are respectively the Pre-Separator (PF), the Main Separator (MF) and the Low Energy Branch (LEB). Each section of the Super-FRS consists of a number of focal planes where tracking detectors and degraders can be placed. The H/D experiments will be performed in the dedicated focal planes of the LEB, namely LF2, LF3, LF4 and LF6 [1]. For more details, see Section 2.
Source: The layout is adapted from the Ref. [4].

new synchrotron (SIS100) [5]. Radioactive beams will be generated in fragmentation and fission reactions at the production target. The Superconducting Fragment Separator (Super-FRS) [3,4] will be used for separation and identification of exotic fragments. The Super-FRS will provide beams of higher purity (thanks to the increased number of dipole stages) and higher transmission (thanks to the wider apertures of the magnets) compared to the presently operating FRagment Separator (FRS) spectrometer [6]. It will be mainly operated as an in-flight separator with the three experimental branches, namely High-Energy Branch (HEB), Low-Energy Branch (LEB) and Ring Branch (RB), serving the different NUSTAR experiments. The general layout and the characteristics of the Super-FRS are shown in Fig. 1.

Both HISPEC and DESPEC will share the same suite of Super-FRS tracking detectors in order to determine energy, mass, charge, velocity and position of beam particles. Optimization of experimental conditions in terms of tracking detector properties is essential. This comprises: efficiency, rate capability as well as the beam envelop. Such quantities can be defined with the use of simulations and are then integrated into the evaluation of the response of the specific experimental array in use (e.g. AGATA, DEGAS, AIDA). As an example, Geant4 simulations of γ-rays (e.g. DEGAS) and charged-particle detectors (e.g. AIDA) need as input the distribution profile of fragments which can be at present only obtained from the customized simulations.

This paper presents selected examples of such simulations in order to highlight the experimental constraints and resulting performances for H/D campaigns. Four sets of simulations are reported:

1. Medium-mass nuclei (A∼100) produced by fragmentation of 1 GeV/u ^{107}Ag on ^{12}C target with ^{84}Mo as central fragment.
2. Heavy mass region (A∼200) populated by fragmentation of 1.5 GeV/u ^{238}U on ^{12}C target with ^{214}Pb as central fragment. Two sub-cases are presented: (a) Setting with the thin wedges. (b) Setting with the thick wedges, and consequently more pronounced charge state contributions as well as lower energy of the fragments at the LF2 focal plane.
3. Heavy mass region (A∼200) populated by fragmentation of 1.5 GeV/u ^{238}U on ^{12}C target with ^{220}Pb as central fragment.

The paper is organized as follows: In Sections 2 and 3 a short description of the Super-FRS and a brief overview of the simulation programs are provided. In addition, features of interest for H/D experiments together with the reconstruction of important simulation parameters are shown. In Sections 4 and 5 the results of simulations are presented and discussed.

2. Super-FRS for H/D experiments

The Super-FRS will be the most powerful in-flight separator in the world. Rare isotopes of all elements up to uranium will be produced at relativistic energies and spatially separated within a few hundred nanoseconds, enabling the study of very short-lived nuclei. The secondary cocktail beams will be then delivered to various experimental areas or fed into storage rings. The relevant parts of Super-FRS for H/D experiments are respectively the Pre-Separator (PF) and the Main Separator (MF), delivering beams towards the Low Energy Branch (LEB), where the H/D setups will be located (see Fig. 1). The separation and the identification of the radioactive fragments will be carried out in the Pre-Separator and the Main Separator of the Super-FRS, by means of their magnetic rigidity and by energy-loss in shaped energy degraders, applying the standard Bρ-ΔE-Bρ method [6] in two stages, in the Pre-Separator and in the Main Separator. The basic ion-optics of the Super-FRS can be found in [15], here we just remind the layout and position of the focal planes, of interest for the discussion afterwards. The Pre-Separator has two deflecting dipole stages with an intermediate wedge-shaped degrader. Each stage comprises a triplet of dipoles, many quadrupoles and higher-order (sextupoles and octupoles) focussing elements. Four focal planes can be identified in the Pre-Separator, PF1-4. The degrader is placed in the PF2 dispersive plane and grants the spatial separation of the nuclei with different atomic numbers at PF4. The Main Separator has four deflecting dipole stages with a wedge-shaped degrader after the first two. Each stage is made of a triplet of dipoles, at least two triplets of quadrupoles and higher-order (sextupole, octupole) magnets. The H/D experiments will be performed in the dedicated focal planes of the LEB, namely LF2, LF3, LF4 and LF6 [1] (for more details, see Fig. 1). There will be two general purpose wedge degraders:

The one in PF2 focal plane (middle dispersive focal plane of the Pre-Separator) will be used to operate the Pre-Separator in achromatic mode, while the one in the MF2 focal plane (middle dispersive focal plane of the Main Separator) will be set to operate the Main Separator in either achromatic or monochromatic mode. An achromatic focus also leads to a minimum position spread at LF2 (in dispersive X plane), while in monochromatic mode instead the energy spread is minimized. The thickness of the degraders has to be carefully chosen to optimize transmission and separation in different focal planes. The settings were calculated to be achromatic/monoenergetic based on imaging of the separator together with calculated energy loss and wedge shape.

With respect to H/D experiments, degraders and detectors will be used at the PF2, PF4, MF2, LF2, LF3, LF4 and LF6 focal planes. For DESPEC experiments an additional degrader is suggested at LF3 focal plane to compensate for the energy loss required at AIDA. For HISPEC it is advisable not to use a degrader at LF3 but to use a thick degrader at the LF2 focal plane instead. The transmission will be much better at higher energy which also keeps the electron capture process in fragments low.

A "FLASH" of secondary radiation (Bremsstrahlung γ-rays, protons, other low energy charged particles) will be produced at high intensity in the final degrader, and could saturate the electronics of HPGe detectors. The FLASH will be observed within a prompt time window (< 50 ns) in the timing spectrum of the HPGe detectors. These background events do not pose significant challenge to DESPEC experiment where the β-delayed γ-rays will be the main interest for investigation in HPGe spectrum. This is one of the reasons for different degrader configurations that has been suggested for the HISPEC and DESPEC experiments.

The principles applied for fragment identification with Super-FRS have the same foundations as fragment identification performed in various previous campaigns at GSI/FRS as well as in other fragment separators at various facilities worldwide.

The identification of the fragments traveling through the Super-FRS is based on the reconstruction of mass and charge state. Basic quantities have to be reconstructed on an event-by-event basis, such as positions at the principal focal planes, time of flight (TOF) between sections and energy losses. In order to extract such quantities specific detectors are placed along the spectrometer. The TOF is extracted from detectors placed at MF2 and LF2 focal planes. The timing detectors are required to have excellent timing resolution (TOF resolution (σ) around 50 ps and better) [16] and to withstand high count-rates (i.e. up to $\sim 10^6$ pps/cm at MF2 focal plane). To cope with such stringent requirements a segmented plastic detector, the so-called FINGER detector [1], is being developed by the H/D collaboration, intended to be used as TOF detector in both MF2 and LF2 focal planes. The FINGER detector will be made of plastic BC420, covering an area of 38×10 cm^2. It will consists of 90 strips, 4.4 mm wide and 1 mm thick (the present FINGER detector consists of 51 strips). The position resolution of the FINGER detector is determined by the size of the strips. For radioactive ion beams at velocities $\beta = 0.8$–0.9 a TOF resolution of 50 ps (and below) is necessary in order to resolve mass number $A \approx 200$ [16]. The time resolution of the FINGER detector directly affects the achievable A/Q resolution. This resolution depends on the rise time of the signal from the plastic scintillator, on the optical systems used to transport the signal to the PMT (i.e. light guide) and on the electronics used to read-out and process the signals. It is expected that new FINGER detector will have a time resolution below 50 ps. Some promising results concerning the possible use of SiPMs (Silicon Photomultipliers) for FINGER detector have been reported in [17]. Due to the radiation damage of the plastic scintillators expected during or after each experiment, it is of utmost importance that the detector strips can be easily replaced. Similarly to the existing detector, the new FINGER detector will have the strips mounted in a frame which can be easily removed and replaced from the top of the chamber holding the mechanical assembly.

The charge (Q) of fragments is deduced using a MUSIC (Multi Sampling Ionizing Chamber) [18] detector with a rate capability of 1

Table 1

Used parametrizations for MOCADI and LISE++ simulations.

Item	Mocadi	LISE++	Ref.
Energy loss and angular straggling	ATIMA 1.4	ATIMA 1.2	[28–30]
Momentum distribution	Goldhaber	Goldhaber	[31]
Mean fragment velocity	Morrissey	Morrissey	[32]
Empirical parametrization of cross section	EPAX3	EPAX3	[33]
Calculation of charge states	GLOBAL	GLOBAL	[34,35]
Masses	AME2012	AME2016	[36–38]

MHz. The specification for Z resolution of the MUSIC detector is 0.2% for ^{238}U, assuming a fragment energy of at least 400 MeV/u at the entrance of the MUSIC detector.

The charge state equilibrium of the ions is achieved by placing stripper foils at different positions. H/D experiments will use Nb strippers positioned behind the target, behind the PF2 wedge degrader and behind the MF2 wedge (more precisely after MF2 detectors). In addition, there will be an additional Nb stripper placed between two gas sections of the MUSIC.

3. Simulation tools

The simulations listed in the Introduction have been performed using two software tools, MOCADI (version 4.2.) [19–21] and LISE++ (version 12.1.2) [22–24], both developed to simulate the transport of nuclei through the separator.

MOCADI is a Monte Carlo simulation program developed for design studies of the GSI fragment separator FRS. It is used to calculate the transport of an ensemble of relativistic ions through ion optical systems taking into account high-order image aberrations (we used 3rd order optics) as well as atomic and nuclear interaction with matter.

The code has a modular structure: different modules consisting of material (target, stripper, detector matter) and optical blocks (dipoles, quadrupoles) are ordered sequentially to reproduce the experimental conditions.

The LISE++ code uses a Gaussian-convolution technique and general polynomial on log scale to determine the overall position, angle and energy distribution of the fragment ions at the various focal planes. LISE++ has also the possibility to perform Monte Carlo calculations. Similarly to the MOCADI code, it has a modular structure. It is important to mention that LISE++ uses only 1st order optics. The LISE++ code is also used to simulate the production and separation of the radioactive ion beams in fragment separators at various facilities worldwide, such as GSI-FRS, RIKEN-RIBF (RIKEN-Radioactive Isotope Beam Factory) [25], GANIL (Grand Accélérateur National d'Ions Lourds) [26] and FRIB (Facility for Rare Isotopes Beams) [27].

A convenient feature of LISE++ is the high simulation speed for fragments production and transmission calculations, due to the aforementioned general polynomial on log scale and Gaussian convolution technique.

This feature was used to assess the total rates in focal planes. Taking into account detector rate constraints, slit aperture values were set. The same slit aperture values were then used in MOCADI simulations. One has to note that in both simulation programs values of target thickness and stripper thickness as well as the slit aperture values were set to fulfill the following criteria: the transmission of fragments of interest should be maximized (retaining sensitivity and selectivity) as allowed by counting rate limitations and following the minimum energy constraints of certain detectors as well as the fragment energy required by the H/D experiments.

Parametrizations used for MOCADI and LISE++ simulations are summarized in Table 1.

In MOCADI simulations realistic experimental conditions for particle identification are implemented. 10000 ions of primary beam were simulated.

3.1. Reconstruction of X, angle, A/Q and Z

The Super-FRS tracking detectors will provide unambiguous event by event identification of the primary fragments. The charge Q and mass number A will be identified using the $B\rho$-ΔE-TOF method. The final aim of the simulations is to reconstruct particle identification plots (PID) where the atomic number Z is plotted against the quantity A/Q. Such quantities are extracted by the following equations:

$$\beta = \frac{L}{TOF \cdot c}, \tag{1}$$

where β is the velocity of the fragment relative to the velocity of light c, L is the flight-path length between TOF detectors at MF2 and LF2 focal planes and TOF is the corresponding time of flight.

$$\frac{A}{Q} = \frac{B\rho}{\beta\gamma cu}, \tag{2}$$

where Q is the atomic charge, A is the mass number, γ is the Lorentz factor, u the atomic mass unit, B the magnetic field and ρ the curvature of the trajectory.

The $B\rho$ for the non-central fragments are calculated from the $B\rho_0$ central fragment using the following relation:

$$B\rho = B\rho_0 \cdot (1 + \frac{X_{LF2} - M \cdot X_{MF2}}{D}), \tag{3}$$

being M and D the magnification and dispersion between MF2 and LF2 focal planes. In order to get an optimal mass resolution, the measured TOF has to be corrected for the position and angle of the fragments with respect to the beam direction. For this purpose TPC (Time Projection Chambers) detectors [39] will be used as primary position detectors at MF2 and LF2 focal planes. The positions X_{LF2} and X_{MF2} are obtained event by event from the TPCs (or from the FINGER detector at MF2 focal plane and TPCs at LF2 focal plane in certain cases) at the respective focal planes. It is to note that the FINGER detector is not foreseen as primary position detector at MF2, nevertheless if necessary (in case of high rates) it can also be used as such but with somewhat limited A/Q resolution. The energy loss in the MUSIC detector is then used for the ΔE measurement to identify the Z of the fragments. A pair of TPCs at the MF2 and LF2 focal planes were used to simulate position and angle measurements. In addition, for some cases, FINGER detector was used to simulate the position at the MF2 focal plane. The requirement for TOF resolution was 50 ps and is used in MOCADI simulations. The requirement for the position resolution of TPC is 1 mm (σ) and is used in MOCADI simulations. In MOCADI simulations, an approximation has been made by assuming that the Z resolution is constant (for all fragments of interest, regardless of a mass region) and equal to 0.2%. The charge state equilibrium of the ions is achieved by placing stripper foils at different positions. However, one has to note that in MOCADI simulations the charge distributions were not recalculated after ions have passed each single layer of matter (e.g. detectors, degrader *etc.*) but only after ions have passed the corresponding stripper section. Ions have been assigned new charge state according to the probabilities calculated by GLOBAL [34,35]. The code GLOBAL can predict the evolution of charge-state distributions in layers of matter for heavy ions ($Z_{projectile} >= 28$) in the required energy range from 80 to 1000 MeV/u and was therefore very well suited for our applications. The code solves the rate equations numerically with electron stripping and capture cross sections up to the M shell with screening effects. In general charge-changing processes of highly charged projectiles during their passage through matter are well understood in the wanted energy and target material range. Limitations of the involved theory at lower energy with more electrons involved can be overcome by taking into account an abundant set of measured data.

The TOF resolution of 50 ps (σ) was used in MOCADI simulations. The $B\rho$ of the central fragments ($B\rho_0$) are obtained from MOCADI. Corrections for additional path length traveled by the non-central fragments is obtained by incorporating the position and angle information at the focal planes and was incorporated into the simulations using MOCADI. The global transfer matrix elements from MF2 to LF2 focal planes are used for this purpose. The assumptions, criteria and parametrization used for LISE++/MOCADI simulation are based on the vast experience from simulating experiments at FRS. The simulations are tailored to Super-FRS and corresponding detectors. One has to note that this paper is the first paper of H/D collaboration with in-depth, detailed and systematic approach to LISE++/MOCADI simulations of certain physics cases.

4. Results

The production and identification of fragments in the Super-FRS have been simulated using the previously described LISE++ and MOCADI software packages.

Four sets of simulation are presented, one in medium mass region (A~100), centering on ^{84}Mo, and three in heavy mass (A~200) neutron-rich region, with a focus on ^{214}Pb and ^{220}Pb.

In the first case, ^{84}Mo is produced following relativistic fragmentation of ^{107}Ag onto a ^{12}C target. This set of simulations shows a typical case used to define performances requested for DESPEC experiment, in which radioactive ion beams are stopped in an active stopper (i.e. AIDA) and their subsequent decay is measured via position and time correlations with the implanted nuclei. Key physics information obtained in this type of experiments are: particle decay branching ratios, first excited states, half-lives and isomeric decays. The technique is very sensitive allowing to study nuclei produced at intensities of the order of $10^{-5} - 10^{-3}$ ion/s [2].

The heavy-mass region of neutron-rich nuclei beyond ^{208}Pb is particularly interesting for nuclear spectroscopy studies: it is a testing ground for shell model calculations, being just outside a double shell closure, therefore allowing to perform a detailed analysis of the nuclear Hamiltonian in heavy systems. In addition, this region is also of significant importance for the study of the stellar nucleosynthesis of heavy elements, up to uranium. The synthesis of these isotopes is due to the rapid neutron-capture process (r process) [40] which is expected to occur in several astrophysical objects, including supernovae and neutron-stars mergers (see Ref. [41] and references therein). The velocity and exact path of the process depend crucially on the nuclear structure of the involved nuclei as well as on their β-decay lifetime.

The second and third sets of simulations aim at defining parameters for a typical HISPEC experiment, where excited states are populated via secondary reactions. In order to do so, selection and transport of species of interest and clear reconstruction of incoming and outgoing fragments is needed to identify the reaction mechanism. Two possible solutions for the selection and transport of nuclei around ^{214}Pb are discussed. This region can be accessed by fragmentation of ^{238}U onto ^{12}C target. The transport is optimized for nuclei around ^{214}Pb.

In the end, simulations for a case which is out of reach in the actual GSI facility will be presented. This will be addressed once the full power of the FAIR accelerator complex will be achieved. The ^{220}Pb case, for which no nuclear-structure information is available, is chosen as example. This is another typical case to be studied using the DESPEC set-up.

The goal of the simulations is to optimize the yield, energy and distribution of the fragments of interest at the focal planes where the subsequent decay or excitation via secondary reactions will be studied in real experiments. Together with yields, selectivity and sensitivity are also crucial parameters to define. For all simulations, the in-flight separation is achieved by using two degraders at the PF2 and MF2 focal planes. Simulation parameters for all four cases are summarized in Table 2. In the case of ^{214}Pb simulations using two different thicknesses of the wedges, as shown in columns 3 and 4 of Table 2 are performed. The setting with a thinner wedges is referred to as the ^{214}Pb$^{(a)}$ case, while the setting with the thicker wedges as ^{214}Pb$^{(b)}$ case. Details are given later in the text.

Table 2
Parameters for the four sets of simulations described hereafter: Target thickness, incident beam species, energy and intensity, mode of operation of the Main Separator (achromatic/monochromatic), thicknesses of wedges and degraders, as well as slit-aperture values in corresponding focal planes are shown.

Item	^{84}Mo	^{214}Pb$^{(a)}$	^{214}Pb$^{(b)}$	^{220}Pb
Primary beam	^{107}Ag	^{238}U	^{238}U	^{238}U
Target thickness [g/cm^2]	5	5	5	5
Beam energy [GeV/u] and beam intensity [pps]	1/10^{11}	1.5/10^{11}	1.5/10^{11}	1.5/10^{11}
Achromatic/Monochromatic setting	Monochromatic	Achromatic	Achromatic	Monochromatic
Wedge thickness at PF2/MF2 [g/cm^2]	3.0/3.0	3.0/2.7	4.8/4.4	4.8/4.8
Homogeneous Al degrader thickness [g/cm^2] first part/second part	3.55/0.81	5.70/0.00	2.20/0.00	2.30/0.48
Slit aperture values, beam blocker [mm]	−90/60	−55/50	−55/50	−80/105
Slit aperture values, PF4 [mm]	−10/10	−7/7	−7/7	−5/84
Slit aperture values, MF2 [mm]	−190/190	−190/190	−190/190	−190/120
Slit aperture values, LF2 [mm]	−90/150	−9/9	−90/20	−150/130
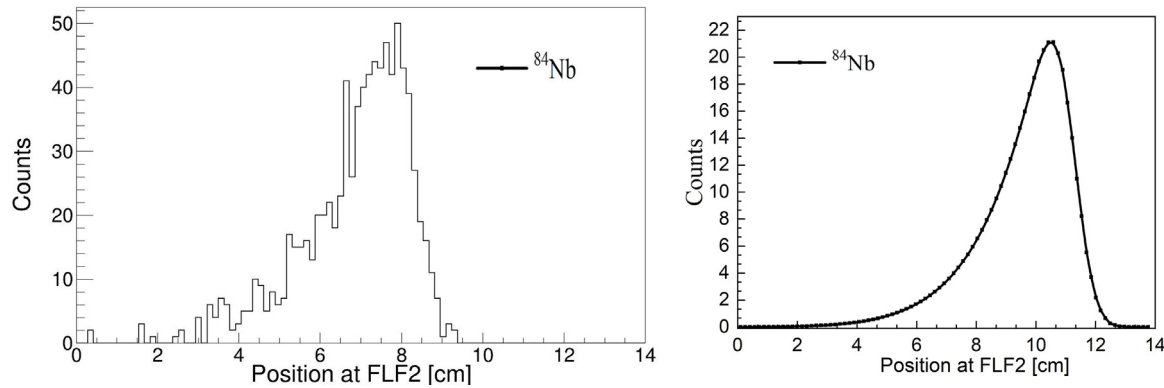
Fig. 2. Simulated X distributions for the non-central fragment ^{84}Nb at LF2 focal plane obtained using MOCADI (*Left panel*) and LISE++ (*Right panel*) packages.

It is important to note that A/Q and Z were calculated for fragments arriving at the LF2 focal point. Since MOCADI provides as output the number of transmitted particles, the yields were normalized using LF2 yields (after the ions pass LF2 slits, more precisely) and target production cross sections. While using in parallel LISE++ and MOCADI simulations inconsistency in the position distributions of fragments in the focal planes was noticed. The difference is most pronounced for non-central fragments, as shown in Fig. 2 where the X-distribution (X is the dispersive plane in our case) of ^{84}Nb in the LF2 focal plane obtained by MOCADI (left panel) and LISE++ (right panel) are compared. The differences just reflect the approximate accuracy one can achieve with simulations and are probably due to the missing higher optics orders in LISE++ and differences in the general approach of treating fragment distributions.

Since the values of slit apertures were taken from LISE++ and simulated Z vs A/Q (ID plot) and A/Q obtained from MOCADI, one has to note that the yields for non-central fragments are to a certain extent approximate. In addition, MOCADI calculates the fragment transmission using a Monte Carlo method and LISE++ using a general polynomial on a log scale and Gaussian-convolution technique instead. A significant difference in transmission of non-central fragments using the two mentioned techniques was noticed. The transmission is a convolution of three effects: target transmission, optical transmission (ion optics of the Super-FRS) and matter transmission (including losses by interaction detectors, strippers, degraders, vacuum windows). A comparison of transmissions of fully stripped ions obtained by MOCADI and LISE++ simulation packages are shown in Table 3. 10000 ions of primary beam were simulated with MOCADI.

Summary of LISE++ "envelope" total rates for all studied cases are shown in Table 4. As expected, there is no contribution from fragmentation → fission in the less fissile, medium mass region. The simulated "envelope" rates (fragmentation and fragmentation → fission) on a FINGER scintillator detector (positioned in MF2 plane) are also shown.

The rates reported are lower than the maximum accepted rates in the different focal planes, being 10^6 pps/cm in MF2, of the order of a MHz in LF2 and lower than 10 kHz on AIDA detectors.

Table 3
Comparison of transmission rates (in %) of fully stripped ions obtained by MOCADI and LISE++ at LF2 focal plane.

Setting	MOCADI	LISE++
^{84}Mo	^{84}Mo 28.8%	^{84}Mo 31.4%
	^{83}Mo 11.3%	^{83}Mo 8.9%
	^{85}Mo 16.1%	^{85}Mo 15.4%
	^{84}Nb 0.8%	^{84}Nb 0.2%
^{214}Pb^a	^{214}Pb 12.9%	^{214}Pb 14.5%
	^{213}Pb 11.8%	^{213}Pb 12.1%
	^{215}Pb 10.6%	^{215}Pb 12.0%
	^{214}Tl 3.6%	^{214}Tl 3.7%
	^{214}Bi 2.3%	^{214}Bi 4.2%
^{214}Pb^b	^{214}Pb 7.3%	^{214}Pb 8%
	^{214}Tl 4.2%	^{214}Tl 4.4%
	^{214}Bi 1.6%	^{214}Bi 3.5%
^{220}Pb	^{220}Pb 5.3%	^{220}Pb 6.8%
	^{219}Pb 4.8%	^{219}Pb 6.2%
	^{220}Bi 1.3%	^{220}Bi 1.7%

Table 4
Total rates (namely, fragmentation reactions and fragmentation → fission) obtained with LISE++ in the four simulations, calculated at FINGER position as well as at LF2 and at stopper/target position.

Rate [pps]	^{84}Mo	^{214}Pb^a	^{214}Pb^b	^{220}Pb
FINGER (MF2) Fragmentation reactions	1.20 ·10^5	3.19 ·10^5	5.31 ·10^4	6.73 ·10^2
FINGER (MF2) Fragmentation → Fission	\	2.19 ·10^4	1.55 ·10^4	\
LF2	5.26 ·10^3	9.06 ·10^3	8.53 ·10^3	91.10
Stopper or target	3.13 ·10^3	4.71 ·10^3	4.54 ·10^3	41.80

4.1. Simulations in medium mass region: ^{84}Mo case

The study of N=Z nuclei is expected to provide the relevant information about the properties of the neutron-proton pairing interaction.

		^{86}Tc 14.7 pps 10.934%	^{87}Tc 0.331 pps 0.006%
^{83}Mo 0.452 pps 5.531%	^{84}Mo 46.1 pps 19.41%	^{85}Mo 891 pps 9.348%	^{86}Mo 108 pps 0.046%
^{82}Nb 48.2 pps 11.32%	^{83}Nb 1580 pps 9.584%	^{84}Nb 382 pps 0.102%	
^{81}Zr 6.6 pps 0.023%	^{82}Zr 47.2 pps 0.008%		

Fig. 3. The quadrant of nuclei of interest populated in the ^{84}Mo setting and impinging onto the stopper (AIDA). The rates (in pps) and transmissions (in %) are shown.

^{84}Mo is an interesting N=Z nucleus, where the existence of a 16^+ seniority spin-trap isomer has been searched for since long [42,43]. This is critical for understanding the shape competition at high spins along the N=Z line and the strong isoscalar interaction between neutrons and protons in the $g_{9/2}$ intruder orbital. This isomer is expected to beta-decay into well-known excited states in the daughter nucleus ^{84}Nb. Such studies motivated the simulation of a possible future DESPEC experiment at the Super-FRS focusing on this nucleus.

In Fig. 3 the region of nuclei of interest impinging on the AIDA stopper (taken into account in this first set of simulations), where the production of ^{84}Mo by fragmentation of ^{107}Ag on ^{12}C target is studied, is reported. Rates (in pps) and transmission (in %) calculated by LISE++ are shown.

AIDA is used in its wide version (24 cm×8 cm in size), arranged in three layers of 1 mm thick DSSSDs. In this simulation the MF2 degrader was set to a monochromatic mode.

Attention is put onto the two "diagonal neighbour" isobars ^{84}Mo and ^{84}Nb with Z differing by one unit, and on "neighbour" isotopes: ^{83}Mo, ^{84}Mo and ^{85}Mo, in order to assess the Z and A/Q resolution capabilities.

The separation of the isobars, obtained by MOCADI simulations, in terms of A/Q (left panel) and in the final ID plot (right panel), is shown in the top row of Fig. 4, where the blue lines (dots) indicate ^{84}Nb and the red ones ^{84}Mo, while that achieved for the mentioned Mo isotopes (^{83}Mo in green, ^{84}Mo in red, and ^{85}Mo in blue) are plotted in the bottom row in the same figure. As expected in these intermediate-mass nuclei, one can observe very clean separation between the nuclei.

Going more specifically to the quantities of interest for the DESPEC decay set-up, one has to focus the attention on the implantation profile of the nuclei in the setting. Using the matter defined in Table 2, one can adjust the degrader in the final focal plane in order to implant ^{84}Mo in the middle of the second stack. By playing with the implantation depth, one could allow also for a correct implantation of ^{86}Mo in the upstream detector, thus expanding the possible scope of the measurement. Experimentally, one could approximately deduce implantation depth by comparing count rates of each detector in the DSSSD stack. By comparing these count rates for different degrader thicknesses with LISE ++ simulations the approximate implantation depths can be deduced.

In the MOCADI simulations the contribution from secondary reactions and charge state distributions were not taken into account. It is expected that less than 1% of ^{84}Mo fragments will change charge states while traversing matter. In order to estimate, instead, the contribution arising from secondary reactions, quite prominent in this region, dedicated LISE++ simulations were performed, which are reported in

Table 5
Total ("envelope") rates for the ^{84}Mo setting, calculated with LISE++.

Rate [pps]	Only fully stripped	Incl. charge states	Incl. secondary reactions
FINGER (MF2)	$1.20 \cdot 10^5$	$1.48 \cdot 10^5$	$2.49 \cdot 10^5$
LF2[a]	$5.26 \cdot 10^3$	$5.77 \cdot 10^3$	$1.12 \cdot 10^4$
Stopper or target	$3.13 \cdot 10^3$	$3.43 \cdot 10^3$	$7.34 \cdot 10^3$

[a]Behind the LF2 slits, before the LF2 degrader.

Table 5: the rates in column 2 are directly comparable to the results of MOCADI simulations, while rates in columns 3 and 4 are calculated including charge states and secondary reactions contributions, respectively. There is a doubling of the total rates between column 2 and 4. The procedure to calculate secondary reactions contributions is based on an iterative method involving a complicated analytical solution as explained in LISE++ paper (see Eq. 5–11 in [24]). The more detailed explanation on the nature of implementation of secondary reactions in LISE++ can be found in LISE++ manual [22].

4.2. Simulations in the heavy mass region: ^{214}Pb case

The region around Pb beyond N = 126 is uniquely accessible at GSI/FRS thanks to the high energy of the primary ^{238}U beam as well as the selection power of the FRS/Super-FRS. These heavy nuclei are an effective testing ground for nuclear models, thanks to the presence of high-j orbitals in an isolated space above the ^{208}Pb core, giving rise to seniority isomers. Isomer decay spectroscopy in neutron-rich lead nuclei, up to ^{216}Pb, has revealed the expected seniority scheme in the $\nu 1g_{9/2}$ shell, with a 8^+ isomeric state, representing the maximum angular momentum achievable by breaking a neutron pair in a j = 9/2 orbital [44]. The lifetime of 8^+ isomeric state has been known for ^{210,212,214,216}Pb (see [44,45] and references therein) while the half-lives of states below the seniority isomers have been known only for ^{210}Pb. This line of research is part of the experimental program of the H/D collaboration to be pursued using beams delivered by Super-FRS. In this section results of two sets of simulations prepared for a future in-beam HISPEC experiment focusing around ^{214}Pb will be presented. In the first case (marked as ^{214}Pb[a] in the text and in Table 2) thin wedges at PF2 and MF2 are used, while in the second case (marked as ^{214}Pb[b]) thicker wedges are simulated. The region of nuclei of interest populated in the two settings slightly differs, as shown by comparison of the plots in Figs. 5 and 6.

When simulating the heavy region of Pb isotopes, an additional complexity arises due to the presence of charge states produced during the transit of the nuclei in the material along the traveling path. The problem is, in fact, more pronounced for heavy isotopes, and couples to a higher request on A/Q resolution. This is particularly pronounced in the second case (^{214}Pb[b]), being the energy at the entrance of the LF2 focal plane lower, as discussed later on. Also for these sets of simulations the attention is focused on isobars (in this case A = 214) and close-lying isotopes $^{213−214−215}$Pb.

At first, the results for sub-set (a) are presented, that is for the use of thin wedges in PF2 and MF2.

The simulated A/Q as well as simulated Z vs A/Q distributions for ^{214}Pb (depicted in red), ^{214}Bi (depicted in blue) and ^{214}Tl (depicted in green) are shown in the top row of Fig. 7. The ion optical setting was optimized for separating the ^{214}Pb as the central fragment along the different stages of the Super-FRS. The achromatic focusing of the fragments at the LF2 focus is ensured by adjusting the thickness and angle of the degrader at MF2 focal plane. The magnetic field applied is determined from the corresponding $B\rho$ value of the central fragment at each stage of the separator. Bottom row of the same figure shows the distributions obtained for ^{214}Pb (depicted in red), ^{213}Pb (depicted in blue) and ^{215}Pb (depicted in green).

Separation of ^{214}Pb, ^{214}Bi and ^{214}Tl nuclei using a FINGER detector as a position detector at the MF2 focal plane is reported in the top

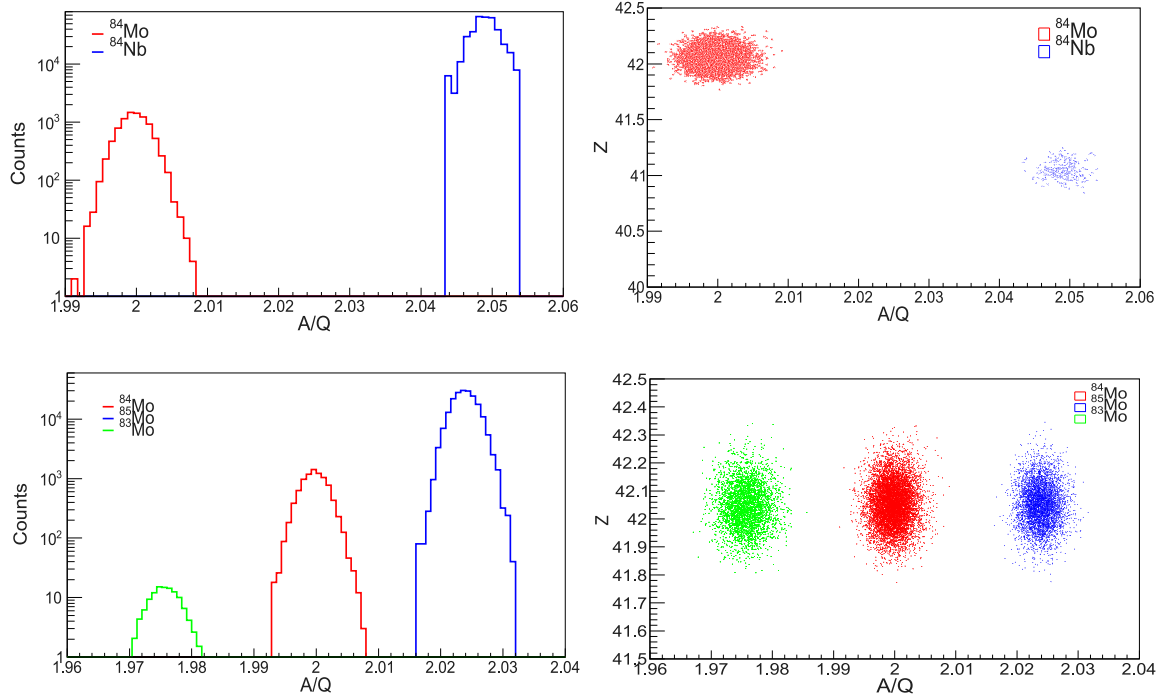**Fig. 4.** Top row: Simulated A/Q distributions (left panel) and ID plot (right panel) for the isobars under analysis: ^{84}Mo (red line and dots), ^{84}Nb (blue line and dots). Bottom row: Same as top row for the isotopes of interest: ^{84}Mo (red), ^{85}Mo (blue) and ^{83}Mo (green). All simulations were performed using MOCADI.


Fig. 5. Quadrant of nuclei of interest populated in the ^{214}Pb$^{(a)}$ setting (thinner wedges) and impinging on the AGATA target. The rates (in pps) and transmissions (in %) are shown.


Fig. 6. Quadrant of nuclei of interest populated in the ^{214}Pb$^{(b)}$ setting (thicker wedges) and impinging on the AGATA target. The rates (in pps) and transmissions (in %) are shown.

row of Fig. 8. The simulated A/Q as well as simulated Z vs A/Q distributions for ^{214}Pb (depicted in red), ^{214}Bi (depicted in blue) and ^{214}Tl (depicted in green) are shown. Bottom row of the same figure

shows the distributions obtained for ^{214}Pb (depicted in red), ^{213}Pb (depicted in blue) and ^{215}Pb (depicted in green). As already mentioned, FINGER detector will consist of 90 strips, 4.4 mm wide and 1 mm
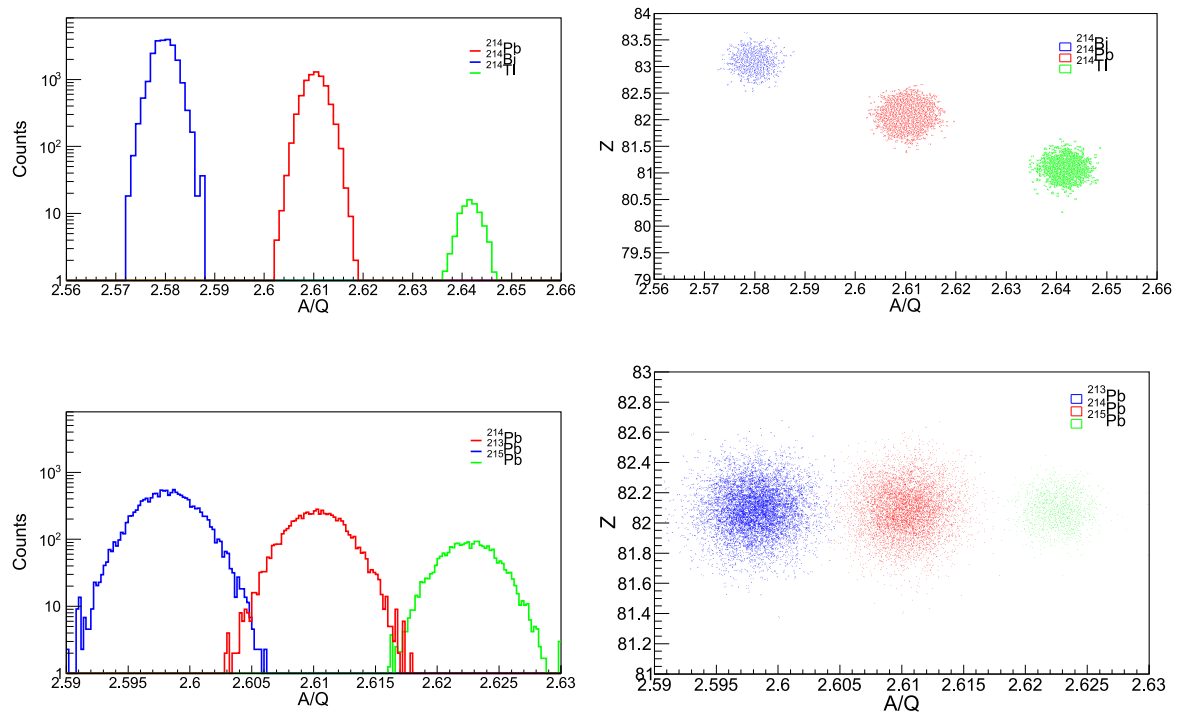
Fig. 7. Top row: Simulated A/Q distributions (left panel) and ID plot (right panel) plots for A = 214 isobars under analysis: ^{214}Pb (red line and dots), ^{214}Bi (blue line and dots) and ^{214}Tl (green line and dots). Bottom row: same as before but for ^{214}Pb (red), ^{213}Pb (blue) and ^{215}Pb (green) isotopes. All simulations were performed using MOCADI.
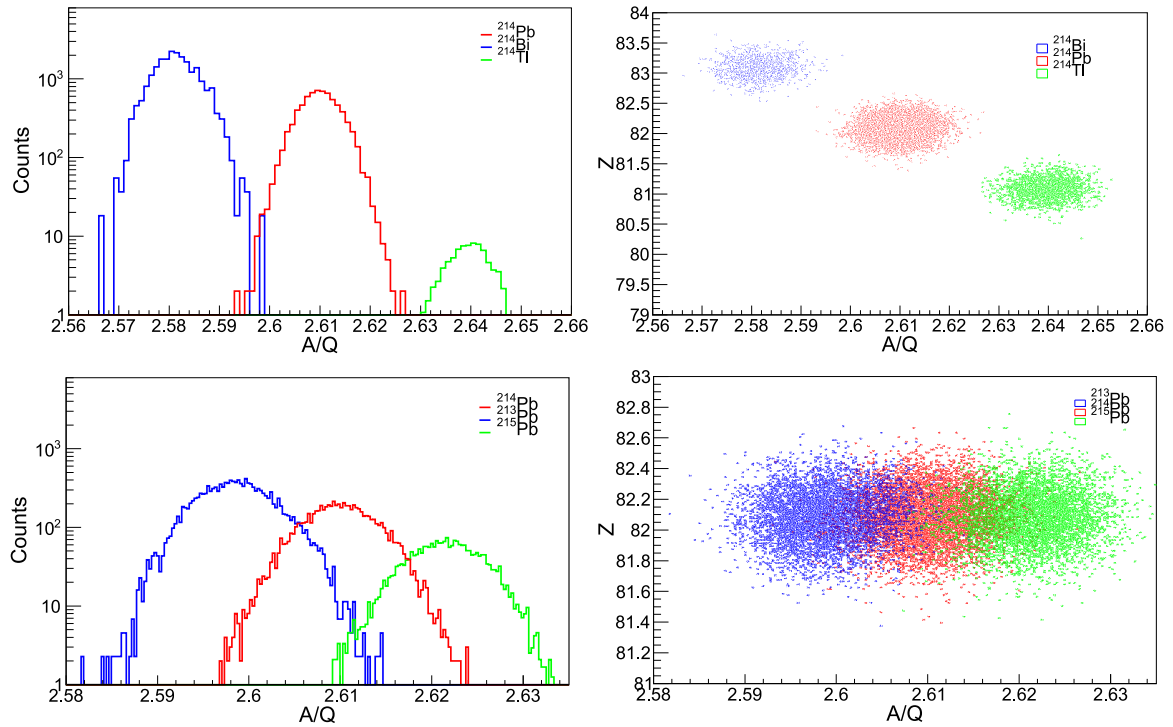
Fig. 8. Top row: Simulated A/Q distributions (left panel) and ID plot (right panel) for A = 214 isobars under analysis: ^{214}Pb (red line and dots), ^{214}Bi (blue line and dots) and ^{214}Tl (green line and dots) using a FINGER detector at the MF2 focal plane. Bottom row: same as before but for ^{214}Pb (red), ^{213}Pb (blue) and ^{215}Pb (green) isotopes. All simulations were performed using MOCADI.

thick. The position resolution of the FINGER detector is determined by the size of the strips. As stated above, the FINGER detector is not foreseen as primary position detector at MF2 focal plane, nevertheless if necessary (in case of high rates) it can also be used as such but with somewhat limited A/Q resolution due to the lower position resolution of FINGER detector compared to TPC detector.

The second case, ^{214}Pb^b, deals with the setting with significantly thicker wedges than the first one.

Simulated A/Q as well as simulated Z *vs* A/Q distributions for ^{214}Pb (depicted in red), ^{214}Bi (depicted in blue) and ^{214}Tl (depicted in green) are shown on Fig. 9. Only the fully stripped and hydrogen-like ($1e^-$ in the atomic orbital) distributions of all fragments have been
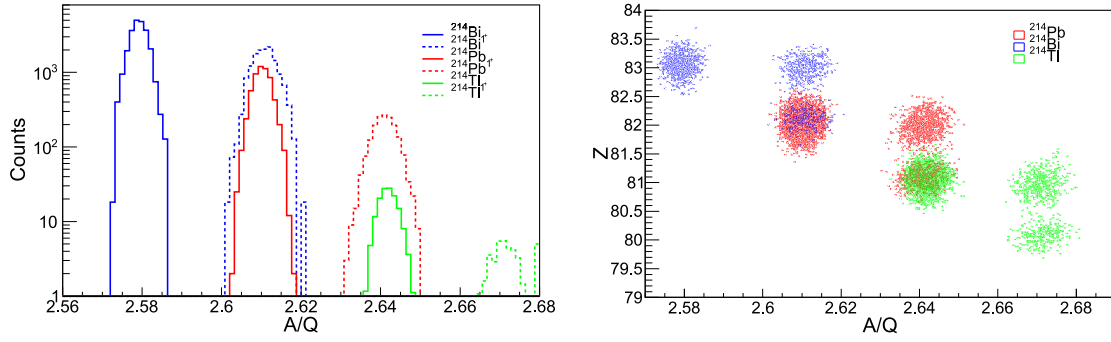
Fig. 9. Simulated A/Q distributions for ^{214}Pb (red), ^{214}Bi (blue) and ^{214}Tl (green). *Right panel*: Simulated Z *vs* A/Q distributions for the same isotopes. See further text for explanation how to separate these fragments.
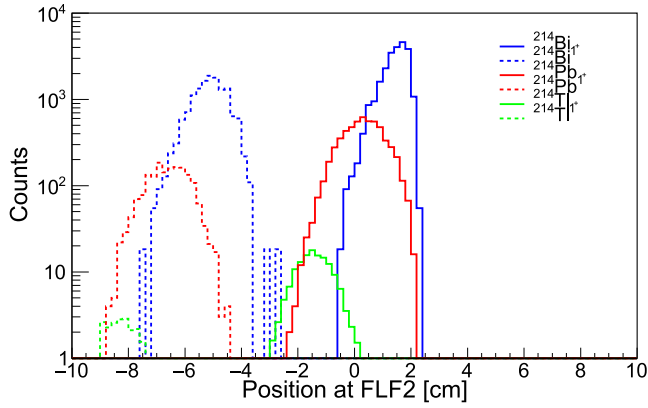

Fig. 10. Simulated distribution of ^{214}Pb (red), ^{214}Bi (blue) and ^{214}Tl (green) fragments at the LF2 focal plane.
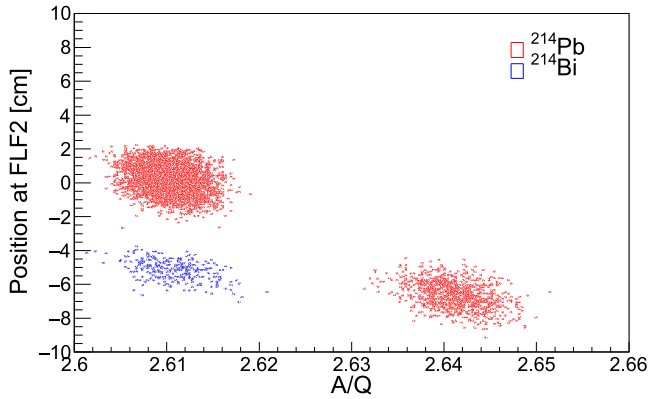

Fig. 11. Simulated Z *vs* A/Q distributions with gate for Z between 81.5 and 82.5 imposed on it (see text for further details).

considered. The simulation has been carried out using an achromatic degrader at the MF2 focal plane. One can see that the production of charge states is, in this case, more pronounced, owing to the lower energy of the fragments. Hydrogen-like fragments are represented with dashed lines in the same color code described above. Strong overlap of the distributions is observed: the hydrogen-like charge state of ^{214}Pb (red) has the same A/Q as the fully stripped ^{214}Tl (green). In addition, the hydrogen-like charge state of ^{214}Bi (blue) is overlapping to fully stripped ^{214}Pb. The intensity of hydrogen-like ^{214}Pb is approximately an order of magnitude less than fully ionized ^{214}Bi, the production of the hydrogen-like ^{214}Bi is approximately an order of magnitude higher than the ^{214}Tl.

The similar A/Q values are due to a fraction of the heavy fully stripped fragments acquiring electrons at the MF2 focal plane. The process of stripping one electron can occur in several stages through the spectrometer, for instance in the Nb stripper foil placed between the two halves of MUSIC detector at LF2. Some of the hydrogen-like fragments which enter MUSIC detector will get one electron removed in the Nb stripper foil. To separate these fragments from the fully-ionized ones the Max($Z1$, $Z2$) is determined within the two sections of the MUSIC detector for each fragment and this value is considered as the Z of the fragment. This however separates only a certain fraction of the overlapping fragments as shown in the Z vs A/Q plot of Fig. 9. The fragments with $Z = 83$, 82 and 81 are identified in three distinguishable regions. One represents fully stripped ion, one represents corresponding hydrogen-like ($1e^-$ in the atomic orbital) fragment and one represents hydrogen-like fragment which got one electron removed in Nb stripper of MUSIC (A/Q is the same as the hydrogen-like fragment, Z=max(Z-1,Z) and is therefore the same as Z of the fully stripped ion).

In order to distinguish the overlapping blue-red and red-green regions of fragments one can use the final arriving positions at the LF2. Simulated distribution of ^{214}Pb (red), ^{214}Bi (blue) and ^{214}Tl (green) fragments at the LF2 focal plane are shown on Fig. 10. One can see that fully stripped and H-like charge states are located at different position at the LF2 focal plane, even if overlapping with each other. A combination of conditions on the two histograms helps, therefore, isolating the contributions of fully-stripped and hydrogen-like ions: a gate on the charge Z between $Z = 81.5$ and $Z = 82.5$, thus selecting Pb only, is imposed and respective fragment positions at LF2 shown in Fig. 11. The overlapping blue–red region is now clearly separated in two regions. The ^{214}Pb and ^{214}Bi fragments are represented with same color as in Fig. 9.

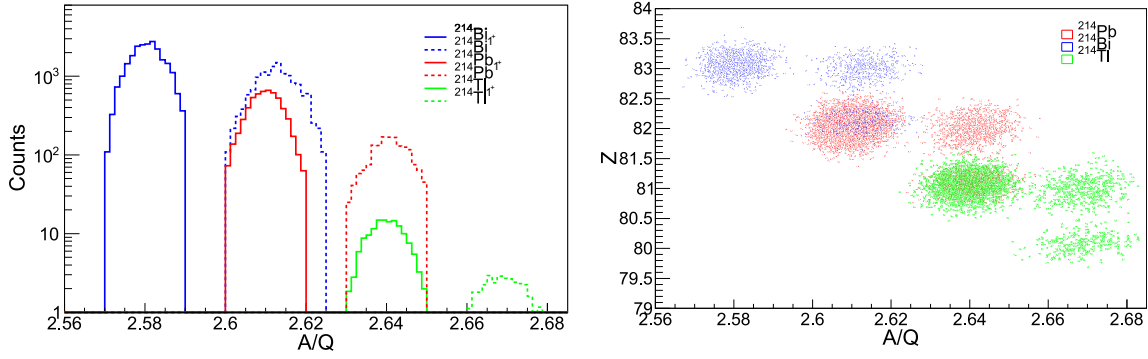Simulated A/Q as well as simulated Z *vs* A/Q distributions for ^{214}Pb (depicted in red), ^{214}Bi (depicted in blue) and ^{214}Tl (depicted in green) using a FINGER detector as a position detector at the MF2 focal plane are shown on Fig. 12.

The population of non-fully ionized nuclei increases, as the ions pass through matter and slow down. The non-fully stripped charge state contribution is observed to be higher for the heavier fragments. One has to note that the calculated LISE++ charge-state contributions depend on both GLOBAL calculations as well as on charge state transmission through the different stages of the separator. Pure GLOBAL calculations (for charge state equilibrium, after passing Nb stripper, as they were used in MOCADI simulations) are shown in Tables 6 and 7.

Secondary fragmentation contamination from the LF2 and LF3 degraders can be removed using energy loss correlation spectra obtained before and after the corresponding degrader. Time Projection Chambers (TPCs) [39] placed at LF2 and LF3 will be used for this purpose.

4.3. Simulations in the heavy mass region: ^{220}Pb

Strongly anticipated cases of FAIR will be physics of very neutron rich nuclei that cannot be accessed using present facilities. One of these

Fig. 12. *Left panel*: Simulated A/Q distributions for ^{214}Pb (red), ^{214}Bi (blue) and ^{214}Tl (green) using a FINGER detector at the MF2 focal plane. *Right panel*: Simulated Z vs A/Q distributions for the same isotopes.

Table 6
The table of charge state contributions during fragment identification process. The quoted values are obtained from GLOBAL code and were deduced for simulations of ^{214}Pb^a case with the thinner wedges. The energy incident on a stripper and charge states distribution after the fragment passes the stripper are shown.

Section	Fragment	Energy [MeV/u]	Fully ionized (%)	Hydrogen-like [%]
After Target+Stripper	^{214}Pb	1156.0	95.8	4.2
At PF2 after wedge and stripper	^{214}Pb	965.3	93.6	6.2
At MF2 after a stripper	^{214}Pb	732.2	87.8	11.8
At LF2 after the first MUSIC gas section	^{214}Pb	660.3	84.4	14.9

Table 7
The table of charge state contributions during fragment identification process. The quoted values are obtained from GLOBAL code and were deduced for simulations of ^{214}Pb^b case with the thicker wedges. The energy incident on a stripper and charge states distribution after the fragment passes the stripper are shown.

Section	Fragment	Energy [MeV/u]	Fully ionized (%)	Hydrogen-like [%]
After Target+Stripper	^{214}Pb	1156.0	95.8	4.2
At PF2 after wedge and stripper	^{214}Pb	854.0	91.6	8.2
At MF2 after a stripper	^{214}Pb	493.3	69.8	27.1
At LF2 after the first MUSIC gas section	^{214}Pb	410.6	56.6	36.2

cases is ^{220}Pb. The heaviest Pb nucleus produced and identified by FRS is ^{218}Pb [45], however no information on its structure is available. No isomeric transitions from ^{218}Pb were observed, but only few hundred ions were accumulated. With an uncertain ion identification, the non-observation is not statistically significant. The ion optics was optimized for separating the ^{220}Pb as the central fragment along the different stages of the Super-FRS. The monochromatic focusing of the fragments at LF2 focus is ensured by adjusting the thickness and angle of the degrader at MF2 focal plane. Calculations simulating a DESPEC experiment making use of AIDA triple (24 cm x 8 cm in size, consisting of three layers of 1 mm thick DSSSDs) will be presented.

The quadrant of nuclei of interest populated in the setting given in Table 4 is shown in Fig. 13, where rates and transmissions are reported. ^{220}Pb implants in the middle layer of the DSSSD stack.

Separation of ^{220}Pb and ^{220}Bi nuclei is reported in the top row of Fig. 14. The simulated A/Q as well as simulated Z vs A/Q distributions for ^{220}Pb (depicted in red), ^{220}Bi (depicted in blue) are shown. The ion optical setting was optimized for separating the ^{220}Pb as the central fragment along the different stages of the Super-FRS. Bottom row of the same figure shows the distributions obtained for ^{220}Pb (depicted in red), ^{219}Bi (depicted in blue). A very clear separation is obtained for the nuclei under analysis, even considering the production of hydrogen-like species.

Separation of ^{220}Pb and ^{220}Bi nuclei using FINGER as a position detector at the MF2 focal plane is reported in the top row of Fig. 15. The simulated A/Q as well as simulated Z vs A/Q distributions for ^{220}Pb (depicted in red), ^{220}Bi (depicted in blue) are shown. Bottom row of the same figure shows the distributions obtained for ^{220}Pb (depicted in red), ^{219}Bi (depicted in blue).

5. Conclusions

The HISPEC-DESPEC experiments will address open questions in nuclear structure, reactions and astrophysics in FAIR. In order to carefully plan the day 1 experiments, robust simulations have been performed using MOCADI and LISE ++ simulation programs. The experiments pose different needs in terms of fragment energy, distributions as well as detector counting-rate capability and dimensions. Four sets of simulations of future H/D experiments are presented. One in medium mass region (A~100), centering on ^{84}Mo, and three in heavy mass (A~200) neutron-rich region, with a focus on ^{214}Pb and ^{220}Pb. In order to maximize sensitivity and selectivity which are crucial for the study of rare nuclei, important parameters (i.e. target thickness, wedge angle and thickness, slit aperture values) have been carefully tuned, taking into account the predicted count-rate handling capability of tracking detectors. Yield, energy and distribution of the fragments of interest have been optimized at the focal planes of Super-FRS where the subsequent decay or excitation will be studied. The assumptions, criteria and parametrization used for LISE++/MOCADI simulation are based on the vast experience from simulating experiments at FRS. The simulations are tailored to Super-FRS and corresponding detectors. One has to note that this paper is the first paper of H/D collaboration with in-depth, detailed and systematic approach to LISE++/MOCADI simulations of certain physics cases. The simulations provide a first glance into forthcoming H/D experiments at FAIR and provide a starting point for the actual planning and preparation.

As expected for the case of the intermediate nuclei, one observes very clean separation between the nuclei. This set of simulations shows a typical case used to define performances requested for DESPEC experiment, in which radioactive ion beams are stopped in an active stopper (i.e. AIDA) and their subsequent decay is measured via position

		^{218}Po 0.188 pps 0.01%			^{221}Po 2.9 pps 0.003%	^{222}Po 1.61 pps 0.001%
			^{218}Bi 2.97 pps 0.169%	^{219}Bi 3.68 pps 0.782%	^{220}Bi 2.07 pps 1.203%	^{221}Bi 0.643 pps 1.152%
	^{215}Pb 0.808 pps 0.003%	^{216}Pb 1.76 pps 0.52%	^{217}Pb 1.72 pps 1.583%	^{218}Pb 1.08 pps 2.845%	^{219}Pb 0.514 pps 4.258%	^{220}Pb 0.161 pps 4.679%
^{213}Tl 0.328 pps 0.053%	^{214}Tl 0.614 pps 0.729%	^{215}Tl 0.567 pps 2.123%	^{216}Tl 0.316 pps 3.421%	^{217}Tl 0.136 pps 4.632%		
^{212}Hg 0.118 pps 0.488%	^{213}Hg 0.106 pps 1.574%	^{214}Hg 0.07 pps 3.03%	^{215}Hg 0.03 pps 4.481%	^{216}Hg 0.01 pps 4.584%		

Fig. 13. Quadrant of nuclei of interest populated in the ^{220}Pb setting and impinging on a stopper (AIDA). The rates (in pps) and transmissions (in%) are shown.
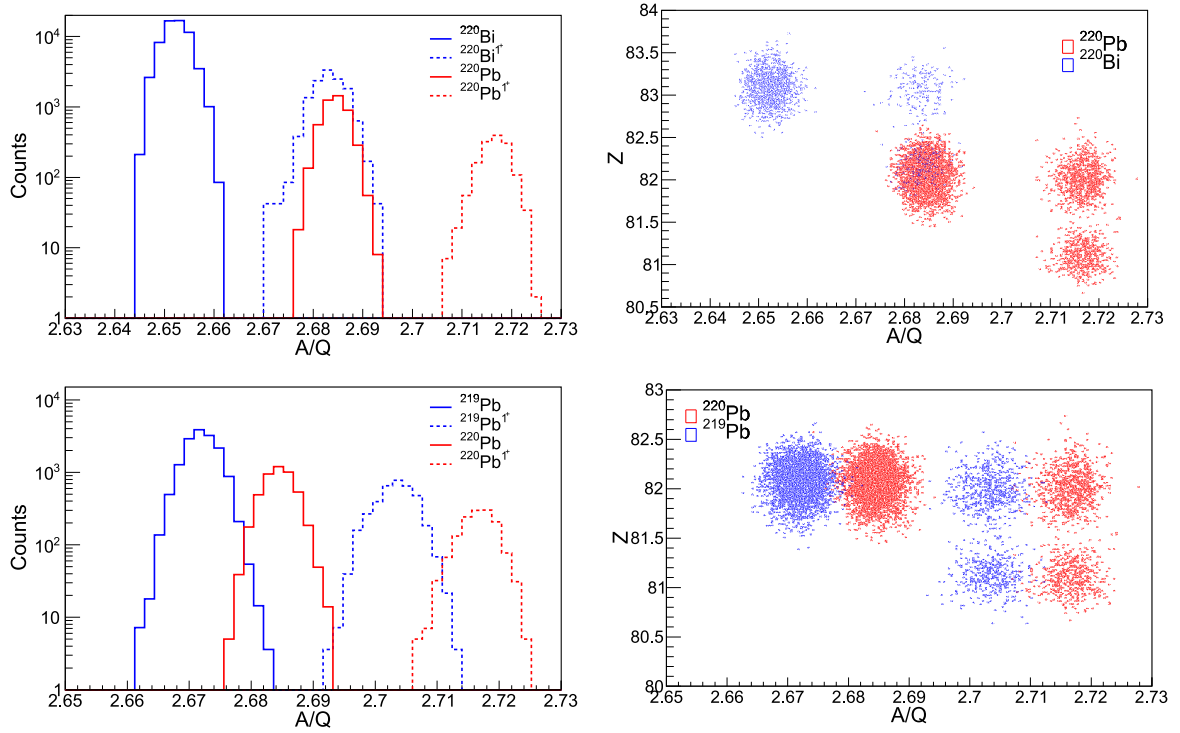

Fig. 14. Top row: Simulated A/Q distributions (left panel) and ID plot (right panel) for A = 220 isobars under analysis: ^{220}Pb (red line and dots), ^{219}Bi (blue line and dots). Bottom row: same as before but for ^{220}Pb (red), ^{219}Pb (blue) isotopes.

and time correlations with the implanted nuclei. While using in parallel LISE++ and MOCADI simulations inconsistency in the position distributions of fragments in the focal planes was noticed. The difference is most pronounced for non-central fragments. The differences just reflect the approximate accuracy one can achieve with simulations and are probably due to the missing higher optics orders in LISE++ and differences in the general approach of treating fragment distributions. Simulation outputs such as fragment position distribution, A/Q resolution and detector rates can be benchmarked in experiments. In that way certain assumptions can be benchmarked and overall simulations improved in the future. The high energy (up to 1.5 GeV/u) of primary ^{238}U and ^{208}Pb beams provided by FAIR will allow the study of nuclei unreachable in any other laboratory. An increase of beam intensities for isotopes far from stability will be achievable with the SIS100 synchrotron and the Super-FRS. The increase in intensity combined with improved separation of Super-FRS and forefront spectroscopy instrumentation, currently realized within the HISPEC/DESPEC project, will enable an outstanding and unique physics program. One of experimental constraints that appear with high primary beam intensities are the high count-rates that detectors have to withstand. To cope with such stringent requirements a segmented plastic TOF detector, the so-called FINGER detector is being developed by the H/D collaboration and is included in simulations. When simulating the heavy region of Pb isotopes, an additional complexity arises due to the presence of charge states produced during the transit of the nuclei in the material along the traveling path. The problem is even more pronounced for heavy isotopes due to the higher request on A/Q resolution. Two sets of simulations prepared for a future in-beam HISPEC experiment focusing around ^{214}Pb are presented. Clear separation is obtained for
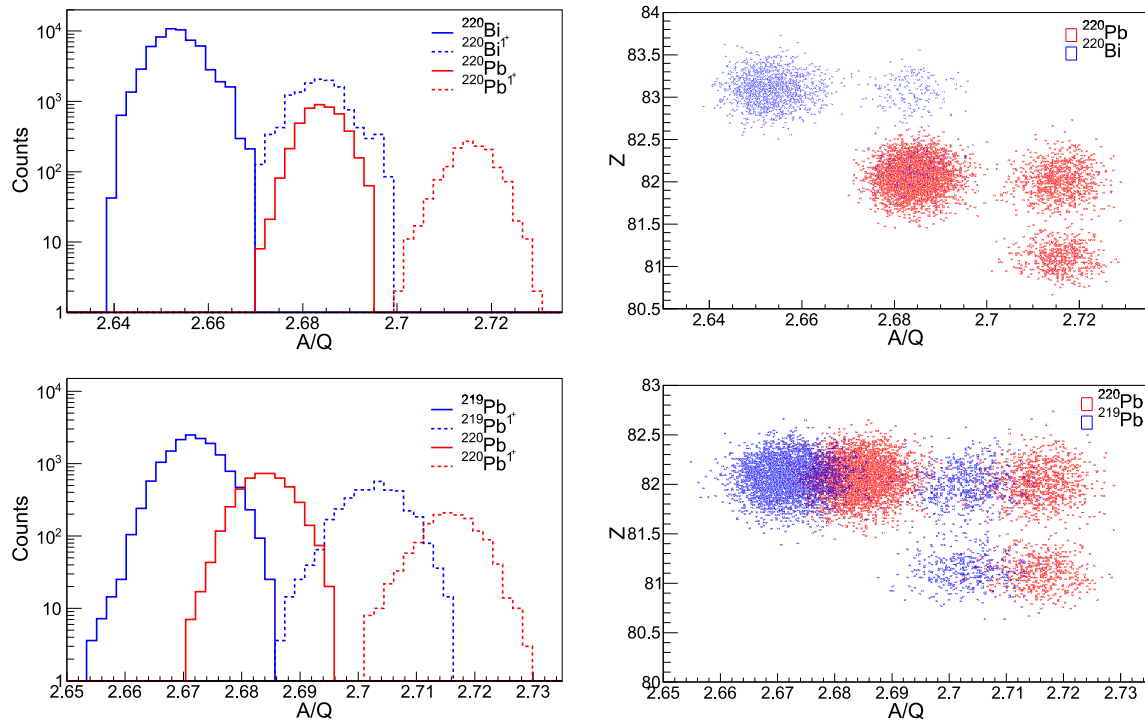
Fig. 15. Top row: Simulated A/Q distributions (left panel) and ID plot (right panel) for A = 220 isobars under analysis: ^{220}Pb (red line and dots), ^{219}Bi (blue line and dots) using a FINGER detector as a position detector at the MF2 focal plane. Bottom row: same as before but for ^{220}Pb (red), ^{219}Pb (blue) isotopes.

the nuclei under analysis, even considering the production of hydrogen-like species. One of the strongly anticipated cases of FAIR is ^{220}Pb. A very clear separation is obtained for the nuclei under analysis. The possibility of production and separation of very exotic neutron rich Pb isotopes for the first time is just an example of exciting physics that is awaiting with FAIR/Super-FRS.

Declaration of competing interest

The authors declare that they have no known competing financial interests or personal relationships that could have appeared to influence the work reported in this paper.

Data availability

Data will be made available on request.

References

[1] Technical report for the design, construction and commissioning of the HIS-PEC/DESPEC beam line, infrastructure and tracking detectors, 2020, https://edms.cern.ch/ui/file/2381481/1/TDR_HISPEC_DESPEC_Infrastructure_public.pdf.

[2] Z. Podolyak, Nucl. Instrum. Methods Phys. Res. B 266 (2008) 4589–4594.

[3] M. Winkler, et al., Nucl. Instrum. Methods Phys. Res. B 266 (2008) 4183–4187.

[4] J.S. Winfield, et al., Nucl. Instrum. Methods Phys. Res. B 491 (2021) 38–51.

[5] M. Durante, et al., Phys. Scr. 94 (2019) 033001.

[6] H. Geissel, et al., Nucl. Instrum. Methods Phys. Res. B 70 (1992) 286–297.

[7] AGATA, in: J. Simpson, J. Nyberg, W. Korten (Eds.), Advanced Gamma Tracking Array, Technical Design Report, 2008, https://www.agata.org/sites/default/files/reports/TDR_EUJRA.pdf.

[8] Technical report for the design, construction and commissioning of LYCCA–the Lund-York-Cologne calorimeter, 2008, https://edms.cern.ch/document/1833842/1.

[9] Technical report for the design, construction and commissioning of the advanced implantation detector array (AIDA), 2008, https://edms.cern.ch/document/1865809/1.

[10] Technical report for the design, construction and commissioning of the DESPEC germanium array spectrometer (DEGAS), 2014, https://edms.cern.ch/document/1813618/1.

[11] Technical report for the design, construction and commissioning of the DESPEC modular neutron time of flight SpectromeTER (MONSTER), 2013, https://edms.cern.ch/document/1833761/1.

[12] Technical report for the design, construction and commissioning of beta-delayed neutron detector (BELEN), 2014, https://edms.cern.ch/document/1865760/3.

[13] Technical report for the design, construction and commissioning of the DESPEC beta decay total absorption Gamma-ray spectrometer (DTAS), 2012, https://edms.cern.ch/document/1812672/1.

[14] Technical report for the design, construction and commissioning of FATIMA, the fast timing array, 2015, https://edms.cern.ch/document/1865981/1.

[15] H. Geissel, et al., Nucl. Instrum. Methods Phys. Res. B 204 (2003) 71–85.

[16] C. Nociforo, JINST 9 (2014) C01022.

[17] M.L. Cortes, et al., Nucl. Instrum. Methods Phys. Res. A 899 (2018) 101–105.

[18] https://www.gsi.de/work/gesamtprojektleitung_fair/super_frs/the_super_frs_machine/components_and_activities/beam_diagnostics/pid/energy_loss.

[19] http://web-docs.gsi.de/weick/mocadi/.

[20] N. Iwasa, et al., Nucl. Instrum. Methods Phys. Res. B 126 (1997) 284.

[21] N. Iwasa, H. Weick, H. Geissel, Nucl. Instrum. Methods Phys. Res. B 269 (2011) 752.

[22] http://lise.nscl.msu.edu/lise.html.

[23] O.B. Tarasov, D. Bazin, Nucl. Instrum. Methods Phys. Res. B 4657 (2008).

[24] D. Bazin, et al., Nucl. Instrum. Methods Phys. Res. A 482 (2002) 307–327.

[25] Y. Yano, T. Motobayashi, Nucl. Phys. News 17 (4) (2007) 5–10.

[26] H. Goutte, A. Navin, Nucl. Phys. News 31 (1) (2021) 5–12.

[27] T. Glasmacher, et al., Nucl. Phys. News 27 (2) (2017) 28–33.

[28] H. Weick, et al., Nucl. Instrum. Methods Phys. Res. B 193 (2002) 1–7.

[29] H. Weick, et al., Improved Accuracy of the Code ATIMA for Energy-Loss of Heavy Ions in Matter, GSI Scientific Report, 2017.

[30] ATIMA web page, http://web-docs.gsi.de/weick/atima.

[31] A.S. Goldhaber, Phys. Lett. B 53 (1974) 306.

[32] D.J. Morrissey, Phys. Rev. C 39 (1989) 460.

[33] K. Suemmerer, Phys. Rev. C 86 (2012) 014601.

[34] C. Scheidenberger, et al., Phys. Rev. Lett. 73 (1994) 50.

[35] C. Scheidenberger, et al., Nucl. Instrum. Methods Phys. Res. B 142 (1998) 441.

[36] G. Audi, et al., Chinese Phys. C 36 (2012) 1287.

[37] G. Audi, et al., Chinese Phys. C 36 (2012) 1603.

[38] W.J. Huang, et al., Chinese Phys. C 41 (2017) 030002.

[39] F. Garcia, et al., Nucl. Instrum. Methods Phys. Res. B 884 (2018) 18–24.

[40] E.M. Burbidge, et al., Rev. Modern Phys. 29 (1957) 547.

[41] T. Kajino, et al., Prog. Part. Nucl. Phys. 107 (2019) 109.

[42] W. Gelletly, et al., Phys. Lett. 253 (1991) 287.

[43] N. Marginean, et al., Phys. Rev. C 65 (2002) 051303.

[44] A. Gottardo, et al., Phys. Rev. Lett. 109 (2012) 162502.

[45] A. Gottardo, Eur. Phys. J. Plus 129 (2014) 9.